

Article

Mineral Fibres and Asbestos Bodies in Human Lung Tissue: A Case Study

Dario Di Giuseppe ^{1,*}, Alessandro Zoboli ¹, Ruggero Vigliaturo ², Reto Gieré ^{2,3},
Maria Paola Bonasoni ⁴, Orietta Sala ¹ and Alessandro F. Gualtieri ¹

¹ Department of Chemical and Geological Sciences. The University of Modena and Reggio Emilia, Via Campi 103, I-41121 Modena, Italy; 176695@studenti.unimore.it (A.Z.); orietta2008@live.it (O.S.); alessandro.gualtieri@unimore.it (A.F.G.)

² Department of Earth and Environmental Science, The University of Pennsylvania, 240 S. 33rd Street, Hayden Hall, PA 19104-6316, USA; ruggero.vigliaturo@gmail.com (R.V.); giere@sas.upenn.edu (R.G.)

³ Center of Excellence in Environmental Toxicology, University of Pennsylvania, 1316 Biomedical Research Building (BRB) II/III, 421 Curie Boulevard, Philadelphia, PA 19104, USA

⁴ Pathology Unit, Azienda Unità Sanitaria Locale IRCCS, I-42123 Reggio Emilia, Italy; paolabonasoni@yahoo.it

* Correspondence: dario.digiuseppe@unimore.it; Tel.: +3905-9205-8497

Received: 2 August 2019; Accepted: 29 September 2019; Published: 8 October 2019

Abstract: One of the open questions regarding the asbestos problem is the fate of the mineral fibres in the body once inhaled and deposited in the deep respiratory system. In this context, the present paper reports the results of an electron microscopy study of both mineral fibres and asbestos bodies found in the lung tissue of a patient who died of malignant mesothelioma due to past occupational exposure. In concert with previous *in vivo* animal studies, our data provide evidence that amphibole asbestos fibres are durable in the lungs, whereas chrysotile fibres are transformed into a silica-rich product, which can be easily cleared. Amphibole fibres recovered from samples of tissue of the deceased display a high degree of crystallinity but also show a very thin amorphous layer on their surface; 31% of the fibres are coated with asbestos bodies consisting of a mixture of ferroproteins (mainly ferritin). Here, we propose an improved model for the coating process. Formation of a coating on the fibres is a defence mechanism against fibres that are longer than 10 μm and thinner than 0.5 μm , which macrophages cannot engulf. The mature asbestos bodies show signs of degradation, and the iron stored in ferritin may be released and potentially increase oxidative stress in the lung tissue.

Keywords: mineral fibre; asbestos; asbestos bodies; SEM; TEM

1. Introduction

Minerals with fibrous crystal habit are widely distributed in the Earth's crust. Among them, the most relevant are commercial fibres that belong to the asbestos family: chrysotile and five amphiboles, *i.e.*, tremolite asbestos, actinolite asbestos, anthophyllite asbestos, crocidolite (fibrous-asbestiform variety of riebeckite), and amosite (fibrous-asbestiform variety of cummingtonite-grunerite) [1–3]. Amphiboles are composed of double chains of corner-sharing SiO_4 tetrahedra with a Si(Al):O ratio of 4:11. The simplified general formula for amphiboles is: $\text{A}_{0-1}\text{B}_2\text{C}_5\text{T}_8\text{O}_{22}\text{W}_2$, where A are cations (Na^+ , K^+ , Ca^{2+} , Li^+) having coordination in the range 6–12; B are irregular octahedral or 8-fold coordinated cation sites content of the so-called $M(4)$ site (Na^+ , Li^+ , Ca^{2+} , Mn^{2+} , Fe^{2+} , Mg^{2+}); C are cations (Mg^{2+} , Fe^{2+} , Fe^{3+} , Mn^{2+} , Mn^{3+} , Al^{3+} , Ti^{3+} , Ti^{4+} , Li^+) that occur in the regular octahedrally coordinated cavities $M(1)$, $M(2)$ and $M(3)$; T are the tetrahedrally coordinated sites within the silicate

chain (Si^{4+} , Al^{3+}); and W are anions (OH^- , F^- , Cl^- , O^{2-}) [3,4]. Chrysotile is a trioctahedral hydrous phyllosilicate based on a 1:1-layer structure with a Si-centred tetrahedral sheet and a Mg-centred octahedral (brucite) sheet, with the ideal chemical formula $\text{Mg}_3\text{Si}_2\text{O}_5(\text{OH})_4$ [5].

Archaeological findings suggest that asbestos fibres were used to create artefacts from a very long time ago [6]. However, the industrial age of asbestos started in the 17th century, when asbestos mining and industrial use began taking advantage of its outstanding technological properties (e.g., flexibility, abrasion and fire resistance, high tensile strength, large surface area, weak sound-transmission coefficient, low thermal conductivity) [2,6]. Thanks to these properties, asbestos fibres were used in more than 3000 industrial applications, including various types of composite products (e.g., asbestos cement), known as asbestos-containing materials (ACMs) [2]. The first studies that suggested a correlation between lung cancer and asbestos exposure date back to the beginning of the last century [7,8]. Subsequently, animal carcinogenicity tests and long-term epidemiological studies provided evidence that inhalation of asbestos fibres, after a latency period of decades, may induce fatal lung diseases, namely malignant mesothelioma (MM) [8]. Following this evidence, the International Agency for Research on Cancer (IARC) classified the six types of commercial asbestos fibres as carcinogenic to humans [8].

Toxicity and carcinogenicity of asbestos are related to their biopersistence, i.e., the ability to persist in the human body despite the physiological clearance mechanisms [9–12]. Biopersistence of mineral fibres is linked to their physical, chemical, structural properties, and biodurability, i.e., the resistance of fibres to chemical/biochemical alteration. The peculiar morphology and length: width ratio (generally >3:1) of mineral fibres make it possible for them to be inhaled and to reach the alveolar region of the lower respiratory tract [13,14]. In this environment, fibres can be engulfed or dissolved by alveolar macrophages [15–17]. Unfortunately, long fibres (length >10 μm) cannot be completely internalised by macrophages and cannot be cleared [12–16]. When the clearance mechanism fails, fibres can be coated with an iron-protein-mucopolysaccharide material, termed “asbestos body” (AB) [9,18–25]. Various models have been postulated to explain the growth mechanism of ABs [9]; however, most of them are based on the physiology of rats [9,18], and therefore, both the actual coating process and the material involved in the development of human ABs are poorly known. Moreover, the influence of ABs on the cytotoxicity of asbestos fibres is still a matter of debate [18–25]. In particular, the potential toxicity of iron associated with ABs should be clarified [6,9,18].

The biological activity of mineral fibres is typically assessed by *in vitro* and *in vivo* studies [13,17,26–29]. Recently, a comparative study on the biodurability of chrysotile and fibrous crocidolite was conducted using human mesothelial and broncho-alveolar cells [27]. In this study, after 96 h of contact with cell cultures, chrysotile fibres were partially dissolved and amorphised, whereas, after the same exposure time, crocidolite fibres showed very minor signs of amorphisation [27]. In the *in vivo* studies, dissolution of mineral fibres was monitored after injection (e.g., intratracheal, intraperitoneal) or inhalation in the animals’ lungs [17,28,29]. Gualtieri et al. [17] reported the results of the first complete and accurate evaluation of biodurability/biopersistence of chrysotile and crocidolite asbestos found in the lung tissue of Sprague-Dawley rats subjected to intraperitoneal/intraleural injection of fibres. Results of the *in situ* morpho-chemical evaluation [17] showed that crocidolite fibres display only a very thin amorphous layer after long contact times (93 weeks), whereas the chrysotile fibres are prone to dissolution, with leaching of Mg and production of a silica-rich relict. *In vivo* tests further showed that formation of asbestos coatings is a common feature in the lungs [9,18]. ABs always coexist with non-coated fibres, which are invariably more abundant than coated fibres [18]. Most coated fibres seem to be amphibole asbestos [18]. ABs tend to form only on fibres longer than 20 μm [25], and therefore, the infrequency of ABs forming on chrysotile core is probably due to the fragmentation of longer fibres into shorter fragments [25].

Even if there is a tradition of excellence in the use of animal models to help in understanding the fate of asbestos in the lung environment [17–25], for human studies the “gold standard” is the *in vivo ex post* lung analysis of human subjects exposed to mineral fibres [6,30,31]. *In vivo* animal studies are of paramount importance for the understanding of asbestos-induced toxicity/pathogenicity, but they are not conclusive because of the differences in the tracheobronchial airway architecture between the

rats and humans [32]. In fact, the differences in the lung geometry can lead to variations in the particle-deposition pattern and hence the site-specific dosage [33]. Moreover, because rats used in *in vivo* tests have a life of about 3 y, the contact time of the fibres with the organic tissue is not comparable to the theoretical residence time of asbestos in the human lung.

The present work reports the results of a combined scanning electron microscope (SEM), transmission electron microscope (TEM), and scanning transmission electron microscope (STEM) study of both fibres and ABs found in the lung tissue of a patient diagnosed with MM who died about 40 y after the first exposure to asbestos. Specifically, the main goals of this study are:

(i) Assessing the biopersistence *in vivo* of the asbestos fibres by scrutinising the variation in the degree of crystallinity and chemical composition of the fibres that have remained in the human lung environment for about 40 y;

(ii) Morphological and chemical characterisation of the ABs found in the lung tissue of the subject. These data are compared with the recently obtained results from an *in vivo* animal test [16,17], in order to acquire more information on the nature and growth mechanism of human ABs and to validate the current knowledge, which is mostly based on animal models.

These data are of paramount importance to unequivocally assess the effect of dissolution and coating processes on the different asbestos species and to improve our knowledge on the fate of these fibres in the human lungs.

2. Materials and Methods

2.1. Description of the Male Subject

Lung-tissue samples were removed over the course of the autopsy of a male subject who was diagnosed with malignant mesothelioma (MM). The patient worked for ten years (from 1970 to 1980) in a factory that produced ACMs and was located in a manufacture district in Northern Italy. Before the ban of all asbestos minerals in Italy in 1992, the company used asbestos fibres for the production of asbestos-containing cement materials, such as pipes and corrugated sheets. In the mixture to produce cement–asbestos, chrysotile represented the most widely used asbestos variety, together with crocidolite until 1986, when the use of crocidolite was banned in the countries of the European Union. Until the early 1970s, the use of amosite was also reported for the preparation of cement–asbestos mixtures. During his occupational activity, the subject was therefore exposed to three asbestos species: chrysotile (major), crocidolite and amosite (minor). From the chronological data of the subject we conclude that the residence time of the fibres in the lung was 37–47 y (average of about 40 y).

2.2. Separation of the Mineral Fibres from the Lung Tissue

Portions of tumour-free tissue of the parenchyma were extracted from the right lung lobe previously stored in formaldehyde solution buffered at neutral pH (Figure 1a,b). To obtain mineral fibres from the lung tissue, sub-samples of 2 cm³ were first freeze-dried using a lyophiliser (Labconco FreeZone, Kansas City, MO, USA) (Figure 1b). Subsequently, the organic matter was oxidised using a low-temperature plasma asher (Emitech K1050X, Ashford, UK) at 80 °C, and with an energy input of 100 W and an oxygen flow of 225 mL/min. Approximately 50 mg of freeze-dried lung samples were ashed [34]. After 20 h, the ash was suspended in a solution made of 50 mL distilled water and 2 mL ethyl alcohol, and then filtered using a polycarbonate 0.2 µm pore-size filter [34] (Figure 1c).



Figure 1. Lung tissue before and after dissolution; (a) parenchyma stored in a formaldehyde solution; (b) lung tissue sub-samples after lyophilisation; (c) filters recovered after low-temperature plasma asher procedure.

2.3. SEM Investigation

SEM analyses were performed at the CIGS laboratory of the University of Modena e Reggio Emilia using a FEI Nova NanoSEM 450 FEG-SEM (Hillsboro, OR, USA) with 15 kV accelerating voltage, 3.5 μ A emission current and 20 nA beam current. Portions of the polycarbonate filters were coated by gold (10 nm of thickness), using a Gold Sputter Coater, Emitech K550 (London, UK), and placed on an Al stub with double-stick carbon tape. The chemical composition of both fibre specimens and ABs was investigated using a XEDS Bruker QUANTAX-200 (Billerica, MA, USA). For the morphometric investigation, each filter surface was examined at different magnification levels, from 1000 \times up to 20,000 \times using 20 SEM images. Length and width of the fibres were measured at different magnification using the ImageJ image analysis software, version 1.52 a [35].

2.4. TEM Investigation

TEM investigations were performed at the Center of Excellence in Environmental Toxicology, University of Pennsylvania and carried out using a JEOL F200 instrument (Tokyo, JP), equipped with a cold field emission gun (CFEG) and operated at 200 kV. The microscope was equipped with two large-area energy-dispersive X-ray (EDX) spectrometers Centurio Silicon Drift Detectors (SDD) (JEOL, Tokyo, JP). A quarter of each filter was washed with 2 mL of acetone in a 15 mL test tube yielding a clear suspension, sonicated 30 s (using a low power sonic bath) and left to set overnight. The following day

a drop of the suspension was transferred onto a 300-mesh carbon copper TEM (Ted Pella Inc., Redding, California, US) grid and left to dry. Unused suspensions and filters were preserved for further sample enrichments, if needed. Observations were made both in TEM and STEM mode to verify the degree of crystallinity and to morphologically characterise the fibres. STEM-EDX was used to determine the chemical composition of, and element distribution in, fibres and AB. The mapping was performed on region of interest (ROI) and the maps were generated after background subtraction on the spectra obtained in the studied ROI. Information on crystallinity and *d*-spacing of the crystalline phases was extracted by taking the fast Fourier transform (FFT) of the high-resolution TEM (HRTEM) images. FFT returns a diffraction pattern of the selected ROI in the HRTEM image. Identification of the phases was achieved by a combination of semi-quantitative EDX analyses and the comparison of the distances between crystal planes (Å) obtained by FFT images with literature reference data. Stability tests were performed by observing the same area for 2 min and checking its morphology as well as its degree of crystallinity during the test and at the end of it (see Figure S1 in the Supplementary Materials). Data analysis was performed using the software ImageJ-3 and Digital Micrograph-4 [35,36].

3. Results and Discussion

Here, we describe morphological, chemical and mineralogical characteristics of the fibres recovered from the deceased subject and then compare the results with those obtained from *in vivo* animal (rat) experiments reported by Gualtieri et al. [17] and Bursi et al. [18]. During these *in vivo* tests, male and female Sprague-Dawley rats underwent a single intraperitoneal/intraleural injection of Union for International Cancer Control (UICC) chrysotile and UICC crocidolite. Animals were allowed to live until spontaneous death. The time elapsed between the injection of the fibres and the death of the animal (expressed in weeks) is considered the residence time of the fibres in the lung.

3.1. Mineral Fibres

In the solid fraction obtained from ashing of the human lung tissue, both non-coated fibres and fibres coated with ABs were found. A total of 52 mineral fibres were examined, of which 31% were coated. The percentage of fibres with ABs detected in the *in vivo* animal study ranged between 3.3% and 5.7% [18]. The coating process in the rat lung appears to be less efficient than in the human lungs. One of the reasons could be the fibre overload in rats' lung tissue, a well-known problem of animal testing using the intraleural/intraperitoneal injection mode [28].

In the examined human lung tissue, SEM-EDX micro-analysis and FFT patterns of non-coated fibres (Figures 2 and S2 in the Supplementary Materials) revealed compositions that are compatible with those of crocidolite (83%) and amosite (7%) (Figure 2d,e). Only one silica-rich fibre, *i.e.*, the metastable product of dissolution of chrysotile mediated by Mg leaching [17], was found (Figure 2f). Identification of coated fibres was difficult since EDX spot analyses were influenced by the presence of ABs. However, the FFT patterns obtained on partially coated fibres (FFT patterns obtained from 10 fibres), combined with STEM-EDX micro-analysis, indicated that crocidolite is probably the main type of coated fibres (Figure S2 and S3 in the Supplementary Materials).

SEM and STEM images of non-coated fibres show quite straight individual amphibole fibres or bundles (Figures 2 and 3). Amosite fibres appear as prismatic individual fibres (Figure 3a). Crocidolite appears as felt-like aggregates (Figure 3b). Fibrils splitting from bundles show a long, thin columnar habit (Figures 2g–i and 3b). Amphibole fibres form both straight edges parallel to the fibre axis and irregular edges (Figure 3), whereas the silica-rich fibre habit appears as curved (Figure 2c). Amphibole fibres show both straight and irregular ends (Figure 3c,d). Amosite shows more right-angle truncations across the fibre axis (Figure 3a) than crocidolite, which tends toward more columnar forms (Figure 3b). The fibres occur occasionally together with other particles, which were identified as residues of incomplete ashing (Figure 2a–c).

The summary statistics of the geometry of the coated and non-coated fibres are reported in Table 1. The data display a wide range of lengths, with values ranging from 2.17 to 107 µm, but the longer fibres predominate in the population. More than 75% of the fibres were longer than 7.45 µm, and 50% were longer than 19.8 µm. The length of crocidolite fibres varied between 2.17 and 107 µm (average

17.2 μm), whereas the amosite fibres ranged in length from 19.49 to 76.4 μm (average 38.5 μm). Although the widths of the fibres ranged overall between 0.06 and 2.82 μm , 75% of the fibres showed a width of less than 0.44 μm . However, all amosite fibres had a width greater than 0.40 μm .

According to the WHO guidelines, asbestos fibres of respirable size with relevant biological activity (so-called “critical” fibres) are those equal to or longer than 5 μm and having diameters up to 3 μm , with an aspect ratio $\geq 3:1$ [14]. All mineral fibres recovered from the lung tissue of the human subject fit the WHO counting criteria concerning both width and aspect ratio, but 15% of the fibres are shorter than the length value set by the WHO.

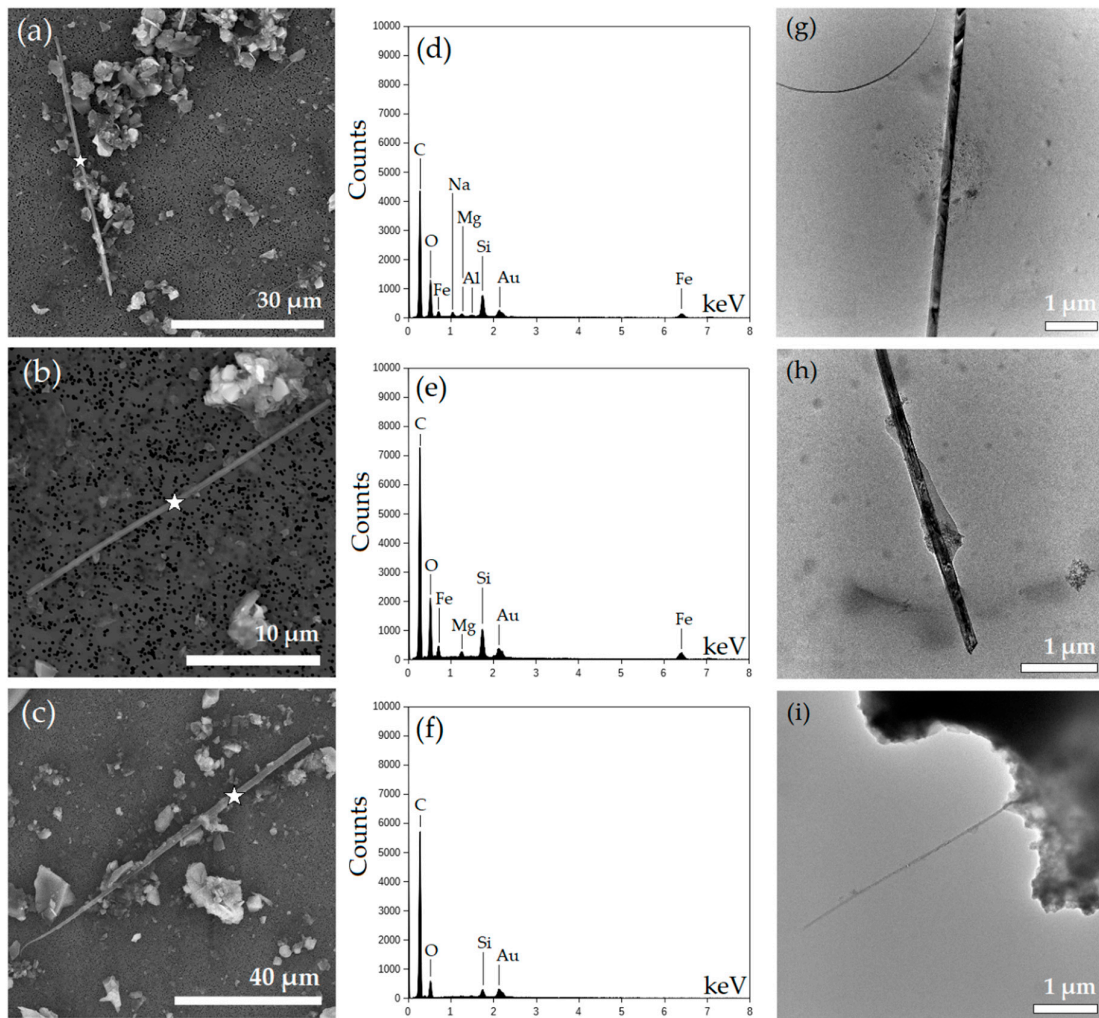


Figure 2. (a) FEG-SEM image of a crocidolite fibre; (b) FEG-SEM image of an amosite fibre; (c) FEG-SEM image of a silica-rich relict of chrysotile; (d) SEM-EDX spectrum of the fibre shown in (a); (e) SEM-EDX spectrum of the fibre shown in (b); (f) SEM-EDX spectrum of the fibre shown in (c); (g) STEM image of an individual crocidolite fibre with columnar habit; (h) STEM images of a prismatic individual crocidolite fibre; (i) STEM image of a thin crocidolite fibre.

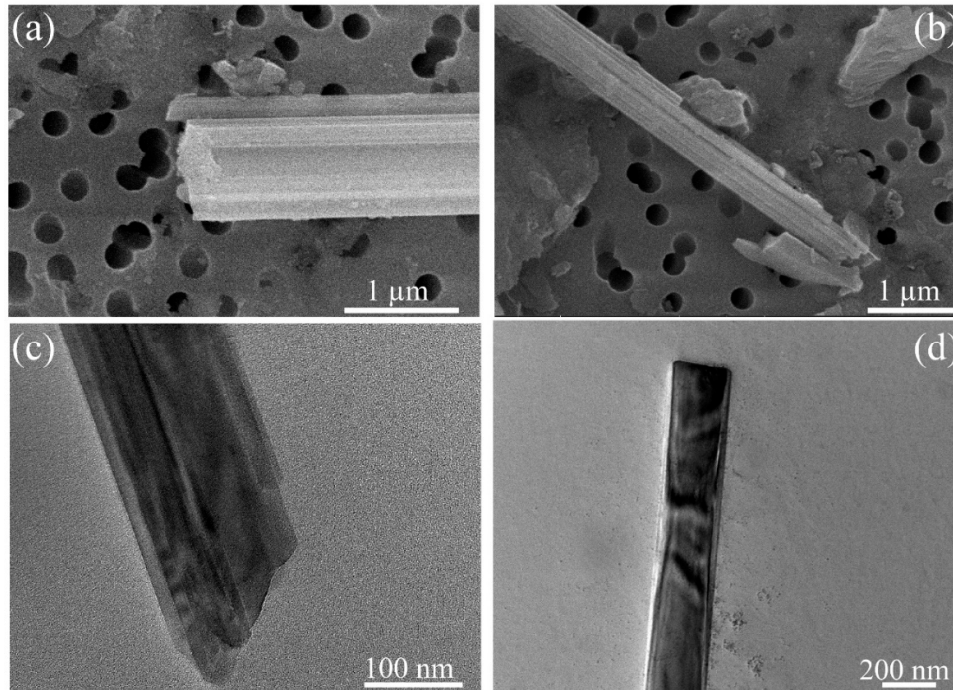


Figure 3. (a) High-resolution FEG-SEM image of an amosite fibre; (b) high-resolution FEG-SEM image of bundles of crocidolite fibres; (c) TEM image of a crocidolite fibre with stepped edges; (d) TEM image of an individual crocidolite fibre showing characteristic diffraction contours.

Table 1. Morphometry of the coated and non-coated fibres recovered from the studied lung tissue. *Percentile indicates the value below which a given percentage of values in a data set fall. L (length); W (width); Min (minimum); Max (maximum); σ_{n-1} (standard deviation).

Morphometry	Min	Percentiles*					Max	σ_{n-1}
		15 th	25 th	50 th	75 th	90 th		
L (μm)	2.17	4.96	7.45	19.8	47.3	61.6	107	26.2
W (μm)	0.06	0.13	0.18	0.28	0.44	0.66	2.82	0.47
L/W	13.5	24.5	29.5	55.2	141	243	601	107

Compared to the morphometric parameters of the asbestos fibres recovered from the rats' lung tissue, the fibres found in the human subject are longer and thinner [18]. After 109 weeks in the lungs of the rats, crocidolite fibres had an average length and width of 13.7 and 0.54 μm , respectively [18]. Crocidolite fibres found in the human lung tissue, on the other hand, display an average length and width of 17.2 and 0.35 μm , respectively. Crystalline chrysotile was not found in the human samples. Nevertheless, as mentioned above, a silica-rich fibre was found, and most likely it represents a relict obtained by dissolution of a chrysotile fibre. This fibre had a length of 99.1 μm and a width of 1.71 μm . Instead, chrysotile was found in the rats' lung tissue after 128 weeks and it exhibited an average length and width of 14.3 and 0.45 μm , respectively.

Figure 4 illustrates the relationship between length (L) and width (W) of all coated and non-coated fibres examined in this study. Only fibres longer than 10 μm and thinner than 0.5 μm were coated by ABs. This peculiarity of ABs to develop only on longer fibres was reported previously for both *in vivo* and *in vitro* studies [17,37]. In Figure 4, values related to non-coated fibres display a wide distribution and a positive correlation ($R^2 = 0.67$) between L and W.

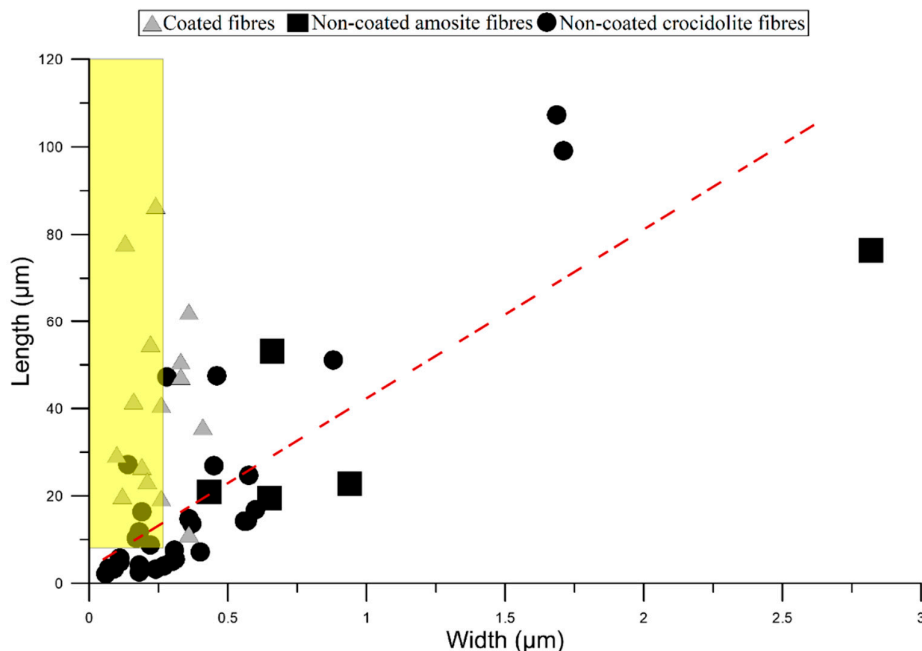


Figure 4. Relationship between the length (L) and width (W) of mineral fibres found in the lung tissue of the male subject. All coated fibres (grey triangles) show $W < 0.5 \mu\text{m}$ and $L > 8 \mu\text{m}$. Values of non-coated crocidolite fibres (black circles) and amosite fibres (black squares) show a straight-line trend (*i.e.*, red dashed line), which is described by the equation $y = 38.9x + 3.40$ ($R^2 = 0.67$). The yellow area marks the L and W values of the “Stanton-size” fibres, *i.e.*, ideally those with $L > 8 \mu\text{m}$ and $W < 0.25 \mu\text{m}$.

Results of SEM-EDX semi-quantitative chemical analysis of non-coated fibres are reported in Table 2. Non-coated amosite and crocidolite show Fe/Si ratios of 1.53 and 2.18, respectively. The reference asbestos amphiboles UICC amosite and UICC crocidolite, on the other hand, have Fe/Si ratios of 0.8 and 0.7, respectively [38].

Table 2. Mean chemical composition and Fe/Si ratio, as determined by SEM-EDX, of non-coated fibres.

Crocidolite	Element Weight Percent					
	Fe/Si	Fe	Si	Al	Mg	Na
Mean (n = 6)	1.53	49.1	33.1	3.12	4.03	10.6
σ_{n-1}	0.45	8.45	3.82	1.54	0.91	5.48
Amosite	Fe/Si	Fe	Si	Al	Mg	
Mean (n = 4)	2.18	60.6	30.7	1.06	6.63	
σ_{n-1}	0.78	9.12	8.26	0.78	1.56	

Figure 5 displays a HRTEM image and the corresponding FFT electron diffraction patterns of a non-coated crocidolite fibre recovered from the lung tissue. The FFT patterns demonstrate that, after several decades of residence in the human lung, the crocidolite fibre preserves its bulk crystallinity (Figure 5a) but exhibits a thin amorphous layer on its surface (Figure 5b). The FFT pattern of the fibre edge (Figure 5b) reveals the characteristic diffuse pattern of amorphous material, whereas Figure 5a shows the typical diffraction pattern of crystalline materials. From Figure 5a, the d -spacings returns a value of 9.9 \AA along (100) and of 5.3 \AA along (001). These values are consistent with the d -spacing of the crocidolite sample reported by Hawthorne [39]. The spatial distribution of Si, Fe, Mg and Na, shown Figure 6, appears uniform along this fibre. The width of the amorphous layer of crocidolite fibres ranges from 3 to 7 nm (Figure 7). The comparison of the results of our HRTEM study with those reported by Gualtieri et al. [17,18] for *in vivo* animal studies [17] shows that after a long contact time

in rat tissue (80 weeks), the mean thickness (15.2 nm) of the amorphous layer developed on the surface of crocidolite was much thicker than that found in our investigations (average 5.12 nm) [18]. Furthermore, the crocidolite fibres found in the lung tissue of the rats, unlike what was found here for crocidolite from human tissue, showed a significant enrichment of Si on the surface of the fibre [18].

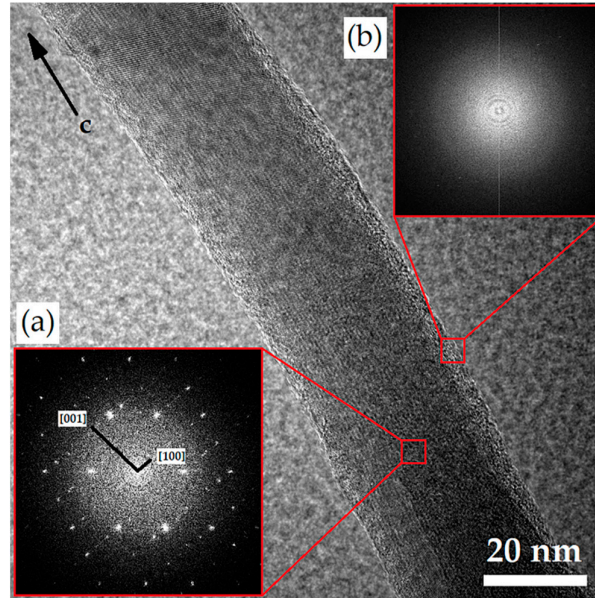


Figure 5. High resolution TEM image of a highly crystalline crocidolite fibre after a residence of ~40 y in the lung of the subject. (a) FFT pattern of the core of the fibre; (b) FFT pattern of the thin amorphous surface layer. The black arrow indicates the direction of the crystallographic c-axis.

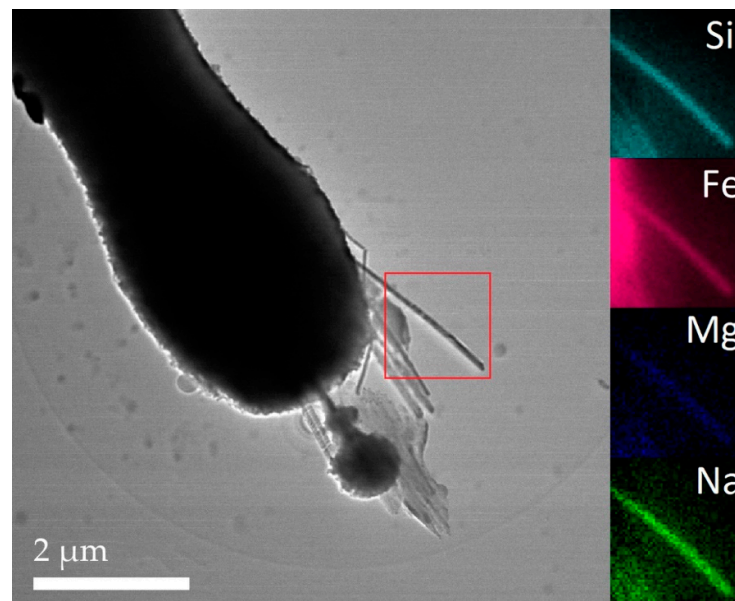


Figure 6. STEM image of crocidolite fibres. The red square identifies the area selected to carry out the EDX mapping. The fibre inside the red square is the same as in Figure 5. The STEM-EDX maps on the right side show the spatial distribution of Si (turquoise), Fe (red), Mg (violet), and Na (green). The maps were generated after background subtraction performed on the spectra obtained in the studied region of interest (ROI).

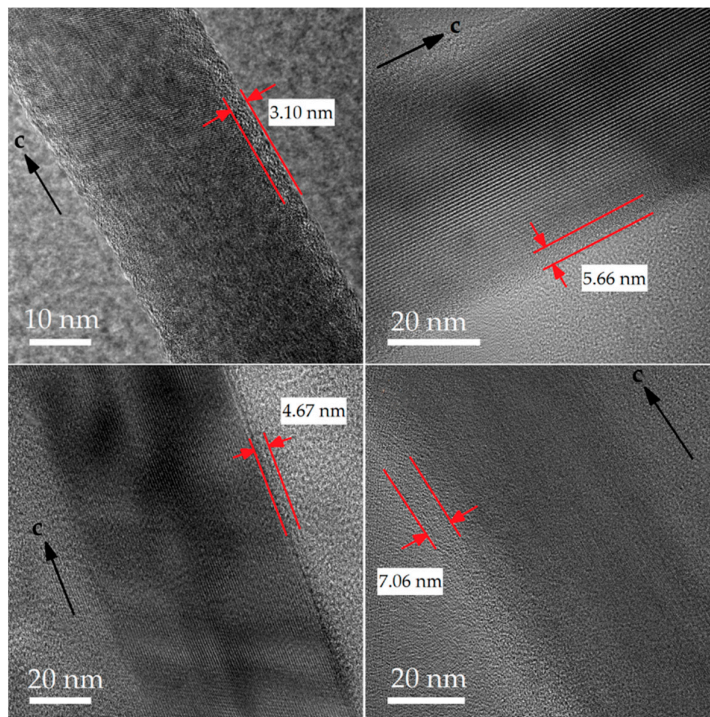


Figure 7. Selected examples (HRTEM images) of four highly crystalline, non-coated crocidolite fibres with a very thin amorphous layer on their surface. Red arrows and red lines highlight the amorphous layer. *c* = *c*-axis of crocidolite. The crocidolite fibre shown in the right top box is the same as shown in Figure 5. The images were acquired after a check of the stability of fibre under an electron beam. The black arrow indicates the direction of the crystallographic *c*-axis.

3.2. Asbestos Bodies (ABs)

In the present work, the term asbestos body (AB) refers to the overall coating material present on the surface of an asbestos fibres. AB segments refer to the individual knobs of the coating material. Fibres coated with ABs were found in all studied tissue samples. FEG-SEM and STEM images document that ABs occur with a wide variety of morphologies (Figures 8 and 9). As mentioned above, the ABs were found surrounding fibres with $L > 20 \mu\text{m}$, but only the fibres with $L > 30 \mu\text{m}$ were completely coated by the ABs. The shape of ABs includes: dumbbell-shaped; beaded; fusiform; elliptical; spherical; cylindrical; and pearl-, lancet- and carrot-like shapes. The beaded structure was the most common appearance of ABs (Figures 8a,c and 9a,e). ABs with beaded structures are variably segmented into spherical or rectangular segments spaced evenly along the fibre. The size of individual AB segments varies in length from 0.2 to 5.0 μm , and width from 0.6 to 4.0 μm . The space between the segments is in some cases covered by a secondary coating (Figure 8a,b). Segments are sub-cylindrical (Figure 8b) or disc-shaped (Figure 9e). Some beaded structures are fused (or partially fused) together (Figures 8d,e and 9c,d,f). The AB segments that occur at the tips of fibres are in many cases sub-rounded, and typically display multiple sequences of coatings (Figure 9a,b). The width of these AB segments at the tip of the fibre range from 1.5 to 9.5 μm . We also measured both the length of the fibres and the volume of ABs and observed that the largest ABs develop on the longer fibres (Figure 10). The volume of ABs was measured on the fibres that were fully visible in the field of view (11 fibres and associated 11 ABs). Depending on the AB form, we used either ellipsoidal, cylindrical or parallelepipedal models to determine the AB volume.

By comparison with our results, the ABs developed in the lungs of rats exhibited various shapes, from cylindrical to elliptical and are often different from those observed here. Globular clusters were present on one or both ends of the coated fibres in the rat tissues. The size of all ABs (including AB segments) recovered from rat tissue varies in length from 4 to 25 μm , and width from 4 to 8 μm . On

the other hand, ABs (including AB segments) recovered from the human tissue samples from this study have lengths between 0.2 to 80 μm and widths between 0.6 to 9.5 μm .

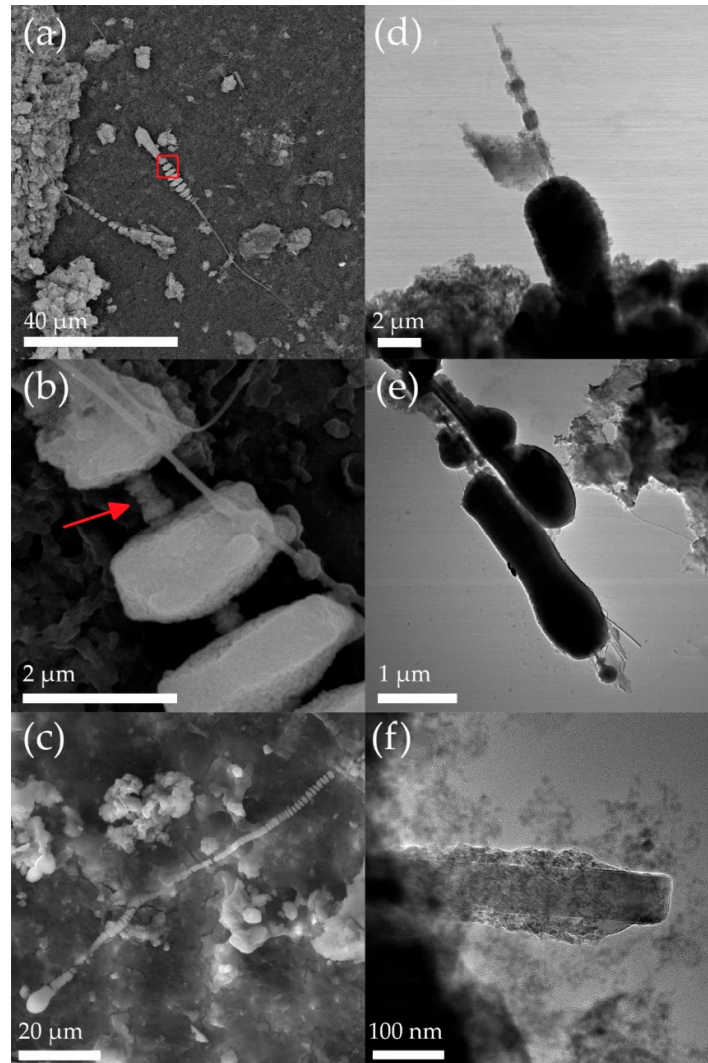


Figure 8. (a) FEG-SEM image showing an example of the beaded shape of asbestos bodies (ABs). (b) Close-up of red square shown in image (a). Image showing the beaded shape with the red arrow indicating the space between individual AB segments covered by a secondary coating. AB segments show sub-cylindrical shape. (c) FEG-SEM image showing the typical beaded shape of ABs. AB and associated fibre cores are curved. ABs show sub-cylindrical segments spaced evenly along the fibre. The AB segment at the fibre tip is sub-rounded. (d) STEM image of a partially coated fibre with elliptical-shaped ABs; (e) STEM image showing a typical example of the apical AB segments at the tips of fibres. Segments are partially fused. (f) TEM image of a partially coated fibre. The AB appears as a smooth, corrugated coating of the fibre.

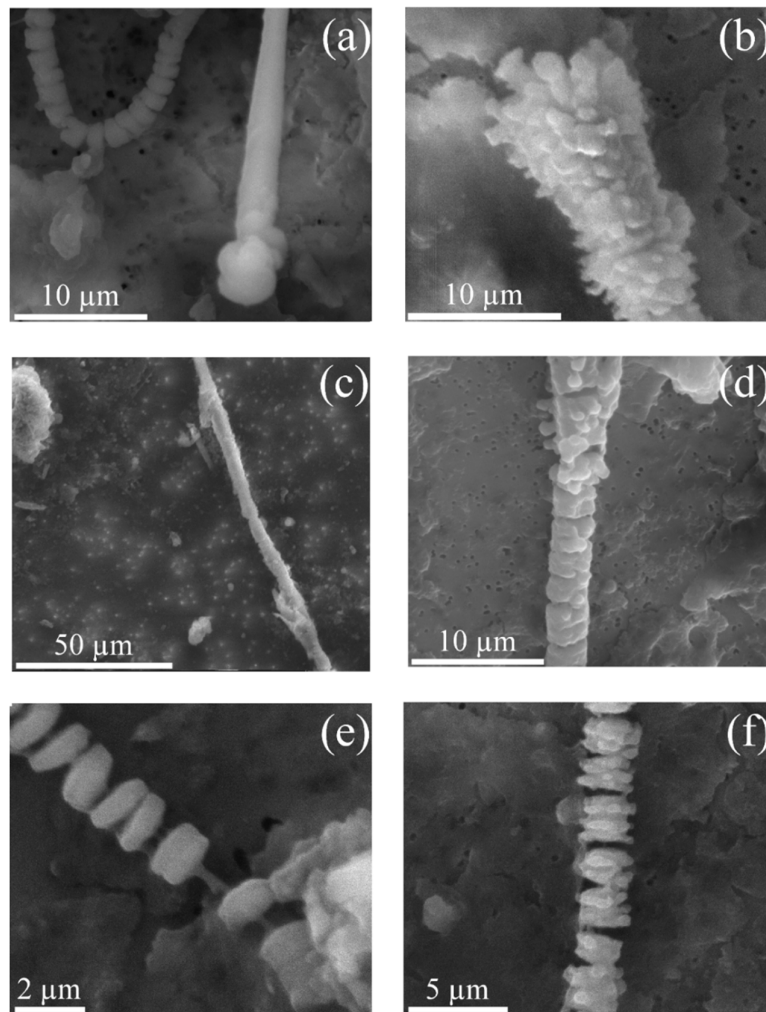


Figure 9. FEG-SEM images of asbestos bodies found in the lung of the human subject. (a) Typical sub-rounded AB segments at the tips of fibres. (b) The AB at the fibre tip showing typical multiple sequences of coatings. (c,d) ABs showing a habit in which the individual segments are fused (or partially-fused) together; (e) disc-shaped beaded segments; (f) disc-shaped segments partially-fused.

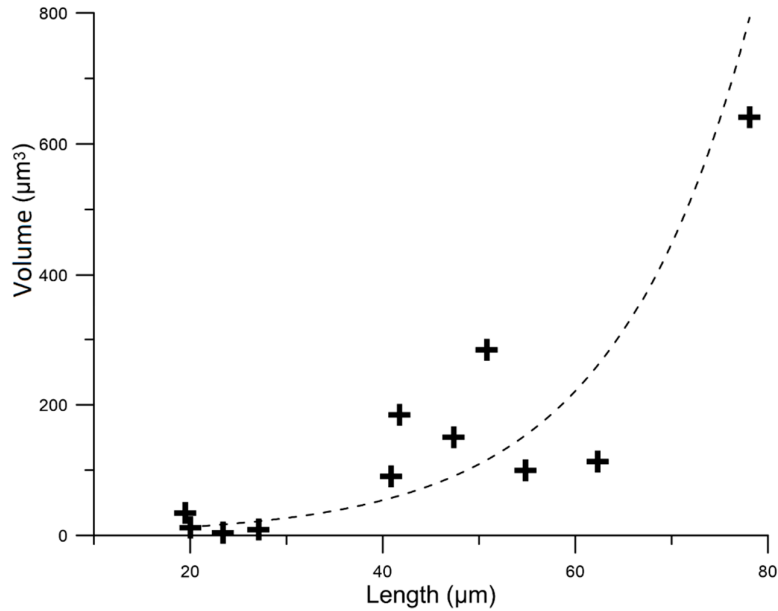


Figure 10. Scatter plot showing the volume of the ABs vs. the length of coated fibres. Dashed line represents an exponential fitting function ($R^2 = 0.70$) to the data points.

The results of semi-quantitative EDX analyses of the ABs are reported in Table 3, together with the elemental composition of ABs developed on a crocidolite fibre found in the lung tissue of another human subject studied by Rinaudo et al. [40]. For comparison, the elemental composition of ABs from crocidolite fibres that were in contact with rat tissue for 80 weeks is also reported (Table 3). The ABs recovered from the human lung tissue are considerably richer in Fe and Si than those recovered from rats which, on the other hand, are richer in Ca and P. Unfortunately, no data regarding the Na, K and Al contents of the rat ABs are available. The ABs investigated here are on average poorer in Ca and Si but richer in P than those studied by Rinaudo et al. [40] (Table 3). The discrepancies between different data sets in Table 3 may be due to the different analytical approaches, detectors and correction factors used by each study.

Table 3. EDX semi-quantitative chemical composition of asbestos bodies. For comparison, data for asbestos bodies recovered from another human subject [40] and from rat lungs (*in vivo* animal tests [18]) are given as well.

Asbestos bodies	Subject	Descriptive Statistics	Element Weight Percent							
			Fe	Si	Mg	Ca	P	Na	K	Al
Present Study	Human	Mean (n = 6)	55.9	19.9	2.58	2.87	11.3	3.20	1.58	3.97
		Max	68.2	41.2	7.85	4.69	24.6	6.16	2.00	7.75
		Min	24.7	6.19	0.64	1.18	1.56	0.30	0.94	0.55
		σ_{n-1}	15.6	13.6	2.71	1.48	8.73	1.96	0.46	2.55
Reference [40]	Human	Mean (n = 3)	41.0	33.7	2.89	5.99	3.94	11.4	1.12	0.82
		Max	53.5	43.9	2.90	6.98	5.70	13.7	1.12	1.31
		Min	28.6	22.8	2.87	4.87	2.52	8.94	1.12	1.16
		σ_{n-1}	10.2	8.6	0.02	0.87	1.32	1.96	-	0.59
Reference [18]	Rat	Mean (n = 11)	4.57	1.82	0.35	16.4	6.99	-	-	-
		Max	10.6	3.86	0.80	21.0	10.3	-	-	-
		Min	1.99	0.99	0.07	8.83	3.46	-	-	-
		σ_{n-1}	2.63	0.98	0.18	4.34	1.99	-	-	-

STEM investigations reveal that the ABs recovered from the lung tissue of the male subject are composed of aggregates of small, rounded particles (Figure 11a,b) with a mean diameter of 52.3 Å ($n = 54$; $\sigma_{n-1} = 4.2$). As reported in the literature [41,42], these particles are mainly composed of ferritin (an Fe-storage protein) or hemosiderin. The nature of hemosiderin is not yet completely understood, but it is believed to be a degradation product of ferritin. It consists of fragments of ferritin usually mixed with other amorphous, decomposed proteins, lipids and/or mucopolysaccharide-based materials [19,42]. An FFT pattern extracted from HRTEM images of ABs revealed the coexistence of a homogeneous halo (due to the presence of amorphous phases) and one to several concentric rings, which arise from the presence of a polycrystalline material (Figure 11c–f). Previous studies [42–45] have shown that Fe is stored inside the hollow cavity of ferritin as ferrihydrite. Ferrihydrite is a poorly crystalline nanomaterial, which can be responsible for the yellow-orange colour of ABs when observed with an optical microscope [46,47]. Ferrihydrite with some degree of crystallinity displays a major diffraction line between 2.5 and 2.6 Å [44] and two minor lines at 1.7 Å and 2.0 Å [47]. In our samples, polycrystalline ferrihydrite was identified because of the presence of the rings at 2.6 Å and at 1.7–2.0 Å in the FFT patterns of the ABs (Figure 11 c–f). Ferrihydrite is a metastable precursor of iron oxides, such as hematite and goethite [45]. The FFT pattern in Figure 11d shows a diffraction ring at 4.2 Å, which may be attributed to (110) of goethite [48]. In Figure 11f, the diffraction ring at 2.5 Å may be attributed to polycrystalline goethite [48]. The coexistence of both ferrihydrite and goethite in the same ferruginous material might result from a catalytic effect of the amphibole surface, where Si-O-Fe connections with ferrihydrite are observed [49]. In fact, these connections are thought to be responsible for the delay in the ferrihydrite–goethite transformation, which extends the stability range of ferrihydrite [50]. It should be noted that great prudence must be taken in extrapolating of FFT results, since ABs are composed of several Fe-based phases, which may have similar crystal-plane spacings contributing to the diffraction patterns. Furthermore, exposure to the electron beam during the TEM analysis may have induced a phase transformation of the studied species/phases. Results of FFT pattern investigation are estimates and do not provide exhaustive qualitative information. The FeOx species should be further investigated with more advanced techniques. ABs may also contain accessory phases, such as apatite or Ca-oxalates [18,40,51]. These accessory phases explain the presence of Ca and P in the spot analyses of ABs (Table 3). Phosphorus, however, can also be present in the protein aggregates. Figure 11c shows a distinctive diffraction ring at 2.7 Å attributed to a major diffraction line of apatite (300), also present as polycrystalline material. In contrast to our findings, a significant number of ABs found in the lung tissue of Sprague-Dawley rats were mainly composed of apatite [18].

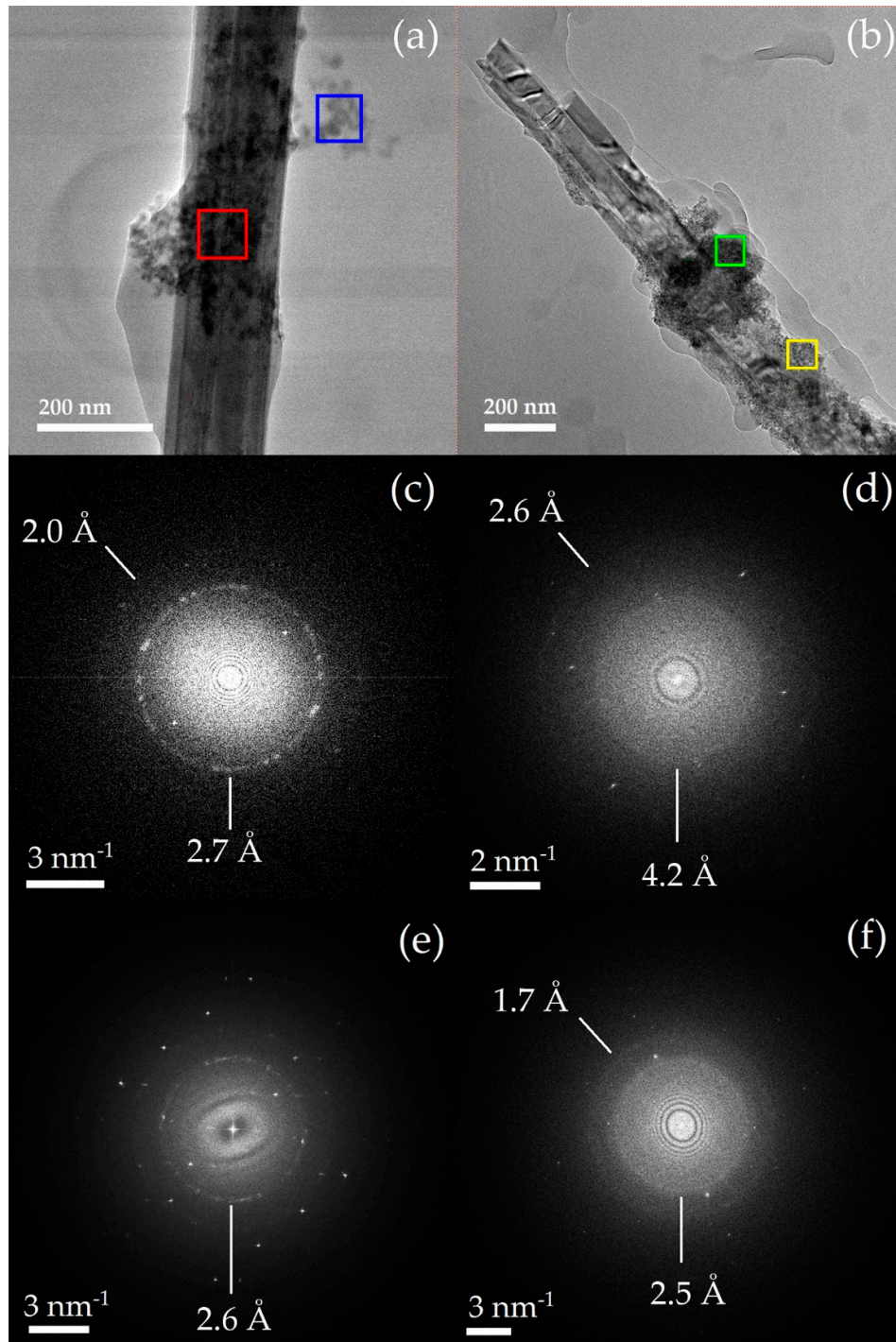


Figure 11. (a,b) TEM micrographs showing ABs on a crocidolite fibre; (c) FFT pattern extracted from HRTEM image of an AB shown in 11a (blue square is the region of interest); (d) FFT pattern extracted from HRTEM image of an AB shown in 11b (green square is the region of interest); (e) FFT pattern extracted from HRTEM image shown in 11a (red square is the region of interest); (f) FFT pattern extracted from HRTEM image of an AB shown in 11b (yellow square is the region of interest). Diffraction rings at 2.6, 2.0 and 1.7 Å may be attributed to ferrihydrite. Diffraction rings at 2.7 Å may be attributed to apatite. Diffraction rings at 4.2 and 2.5 Å may be attributed to goethite.

3.3. Comparison with Literature Data

In the last forty years, several studies focused on asbestos fibres found in lung tissue [52]. One of the universally accepted “reference texts” on this topic is Stanton et al. [53]. According to the so-called “Stanton hypothesis”, carcinogenic asbestos fibres are longer than 8.0 μm and thinner than 0.25 μm (see Figure 4). Following that model, needle-shaped fibres with “Stanton size” cannot be removed by phagocytic cells like macrophages [53,54], triggering the typical asbestos-induced pathological mechanisms (*i.e.*, generation of free radicals, cell and DNA damage, chronic inflammatory reaction, delivery of chemical carcinogens) [15]. Of the amphibole fibres investigated in our work, 75% met the length criteria proposed by the Stanton hypothesis, whereas 50% were thicker than the “Stanton-size thickness”. However, as mentioned above, these models are based on *in vivo* animal studies and are not always suitable for the study of human biomechanisms. In order to accurately identify the dimension of asbestos fibres that are biopersistent in the human lung, Roggli and Green [55] recently examined a wide range of morphologic data for asbestos fibres recovered from lungs of 91 human subjects. A statistically representative processing of this dataset indicated that the majority of amosite and crocidolite fibres that persisted in the lungs after being inhaled have $L > 10 \mu\text{m}$ and $W < 1.0 \mu\text{m}$ [55]. In general, amphibole fibres observed in our investigation met the width criteria proposed by Roggli and Green [55], but only 30% of the amphibole fibres had $L < 10 \mu\text{m}$. As suggested by Roggli and Green [55], these shorter fibres ($L < 10 \mu\text{m}$) should be classified as elongate cleavage fragments with little or no pathogenic effect. This hypothesis is also supported by the work of Berman and Crump [56] that through the statistical processing of the literature data showed that fibres with $L > 10 \mu\text{m}$ contribute most heavily to both asbestos-induced lung cancer and mesothelioma. However, there are still conflicting opinions on this issue and to date there are no conclusive studies proving the non-toxicity or non-pathogenicity of elongate cleavage fragments [57]. The findings of Roggli and Green [55] also confirm the difference between the size of crocidolite and amosite fibres observed in our investigations. Amosite fibres were systematically longer than crocidolite fibres, whereas crocidolite fibres were 30% thinner than amosite fibres.

As proposed by several studies [18,22,55,58] and confirmed by our results, the fibre length plays a key role in the development of ABs (Figure 4). ABs nucleate only at the surface of fibres longer than the Stanton size (Figure 4), which cannot be engulfed by human alveolar macrophages (generally assumed to have a size of $\sim 21 \mu\text{m}$ [59]). These long fibres lead to frustrated phagocytosis and the release of highly reactive cyto- and genotoxic substances into the extracellular space. The formation of ABs represents the product of the exocytotic activity of macrophages aimed at the isolation of these reactive fibres [37]. However, the results of our investigation further suggest that the width of the fibres is also a controlling factor for the formation of ABs. Specifically, only very thin fibres ($W < 0.5 \mu\text{m}$) were coated, and the average width of these coated fibres (0.25 μm) has exactly the same value as that of Stanton-size fibres (Figure 4). It should be noted that some differences found between our results and those obtained in the *in vivo* tests with rats can be attributed to the intrinsic differences between human and other animal cells. For instance, the size of the phagocytes is species-dependent [59,60] and this can undoubtedly influence the formation of ABs.

3.4. New Insights in the Mechanism of Formation of ABs

Asbestos fibres that have managed to pass the upper respiratory system (the first defence mechanism of the body against alien particles) and have been deposited in the alveolar space promptly summon accumulation of phagocytic cells (*e.g.*, macrophages) in charge of dissolution and clearance of the fibres. This second defence mechanism of the body against respirable particles is effective for small spherical objects but fails for longer asbestos fibres. When macrophages fail to completely internalise the longer fibres (frustrated phagocytosis), an inflammatory activity is prompted. This inflammatory activity can become chronic, because fibres can be biopersistent and resist reiterated attempts of phagocytosis. At this stage, the third defence mechanism of the body may take place as “frustrated” phagocytic cells promote isolation of the alien particles by encapsulating them inside the ABs. However, only fibres with the Stanton-type size can effectively undergo this process, which is mediated by Fe [37,53]. Iron can be released during the inflammatory activity, if present in specific lysosomes, and can contribute to the formation of homogeneous aggregates of iron

hydroxide micelles (ferritin or hemosiderin) around the fibres [22,37]. The coating process takes place only where the lysosomal contents (mainly acid hydrolases) are released and accumulate on the fibre surface [37]. Macrophages are supposed to cause a compartmentalised production of ABs, which results in the typical segmented structure [37]. The peculiar sub-spherical structure of ABs is due to the globular shape of ferroprotein complexes, such as ferritin and hemosiderin [42]; *i.e.*, an accumulation of spherical corpuscles (*e.g.*, ferritin micelles) around a cylindrical solid, such as a fibre, generates a rounded coating (AB segments). As clearly demonstrated by *in vitro* and *in vivo* experiments [37,60,61], assuming that abiotic pathways are negligible, the coating process starts as a smooth layer of ferroproteins and later develops into the characteristic beaded structure. The difference in size of the ABs located along the fibre and that of the bulbous ABs at the tip of the fibre has never been considered to date. Time-lapse video microscopy of macrophage–asbestos fibre-binding events [62,63] showed that the macrophages try to internalise the long fibres by preferentially starting from their terminations. Consequently, this portion of the fibre is subject to repeated coatings, leading to increased thickness. Previous studies also state that the pearl structure is the final step of the fibre-coating process [37,58]. However, our observations show that mature ABs can eventually develop secondary coatings that tend to cover the previous, segmented ABs (Figure 9b–d). Figure 12 merges the findings of our study with the consolidated models from the literature [37,60,61] to update the mechanism of AB formation in the human lung. In the first stage of development, ABs appear like a smooth, corrugated coating of the fibre (Figures 8f and 12b). Compartmentalised production of ABs by macrophages then leads to the development of the typical segmented structure (Figures 8d and 12c). Mature ABs show the completely beaded shape (Figures 9e and 12d). During growth, the AB segments at the tip of the fibre incorporate adjacent units and increase in size (Figures 8e and 12d). After remaining in lung tissue for a long time, the ABs may develop multiple coatings (Figures 9b,d and 12e). This phenomenon occurs mostly at the tips of the fibre (Figures 9b and 12e).

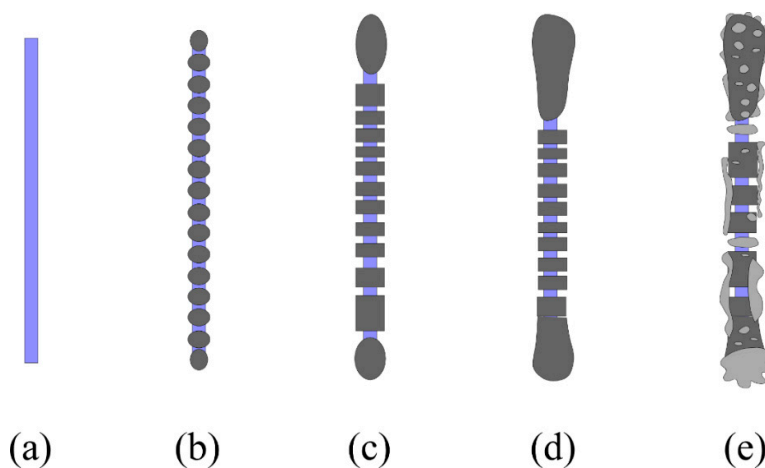


Figure 12. Graphical representation of development of an AB. Mineral fibre is light purple; AB is dark grey; secondary coatings are light grey. (a) non-coated fibre; (b) first stage of fibre coating, AB appears like a smooth coverage; (c) AB evolves developing a segmented structure; (d) mature AB with a pearl structure, where the individual segments are well separated from each other. The ends of the fibre are larger than the other segments and sub-rounded; (e) some fibres may show multiple coatings.

Despite the existence of a large body of literature data dealing directly or indirectly with ABs, the source of the Fe to prompt formation of ABs is still a matter of debate. STEM-EDX chemical mapping (Figure 6) shows that the Fe distribution in the amphibole fibre is preserved, with no or only minor release of Fe outside the structure to act as an iron pool for the formation of ABs. As proven by the FTT patterns, assuming that abiotic processes are negligible, the Fe detected by EDX analyses of ABs is associated with ferroproteins, such as ferritin [64]. Therefore, the open question is why and how macrophages use ferritin to coat the asbestos fibres. Some speculation can be done considering the polyvalent nature of ferritin. Ferritin is a nanobox protein designed to contain and

maintain Fe in solution [65]. In addition, as suggested by Arosio and Levi [66], this protein plays an important role in the protection of cells against oxidative damage. Ferritin inhibits oxidant-mediated cytotoxicity [67] and reduces lipid peroxidation induced by Fenton-type reactions [68]. The proliferation of ferroproteins (*e.g.*, ferritin) in the lungs is regulated by the siderophages (hemosiderin-containing macrophages) [69–71]. Cells exposed to pro-oxidant xenobiotic substances, such as asbestos fibres, induce recruitment of monocytes (*e.g.*, macrophages) and cytoprotective agents (*e.g.*, ferritin) as defence mechanisms (see above). Consequently, it is possible that when a macrophage interacts with a fibre, its affinity with the ferritin (recruited by antioxidant response) prompts a combined action to build the ABs. Other mechanisms may be active in the ferritin adsorption onto the fibre surface (*e.g.*, electrostatic interaction, van der Waals dispersion, solvation) [64]. In this regard, Ghio et al. [72] suggested that positively charged functional groups of ferritin (*e.g.*, ammonium group) can eventually bond with a silanol group located at the fibre surface. In this case, ferroproteins cluster on a portion of fibre with higher concentrations of silanol, leading to the formation of an AB [72]. However, the interaction of ferritin with asbestos fibres is more complex and evolves with time [40,64,73]. A long-term stay of ABs on the fibre surface causes profound alterations of the ferritin. In fact, ferritin of mature ABs shows high degrees of alteration, which can eventually lead to exposure of its ferrihydrite core and a potential release of Fe [73]. In support of this hypothesis, we observed goethite, identified by the FTT patterns (Figure 11), which documents alteration of ferrihydrite while ABs remain in the lung tissue. Uncontrolled release of Fe from ABs into the extracellular space may eventually mediate Fenton-like reactions and generate reactive oxygen species (ROS), thereby increasing oxidative stress.

4. Conclusions

Our investigation provides new insights into the activity of asbestos in the human lung and proves that amphibole fibres can persist unaltered (showing just a thin amorphous coating) in the lung tissue for a lifetime. On the other hand, chrysotile fibres undergo dissolution, with Mg release and production of amorphous silica-rich remnants. In this study, the overall crystallinity of crocidolite fibres has been verified. In a separate study [74], synchrotron nano-diffraction data have shown that amosite fibres recovered from the lungs of the subject investigated here preserve the original atomic distribution in the crystal structure after 40 y of residence in the lungs. Here, 75% of the mineral fibres (coated and non-coated fibres) were longer than 5 μm and thinner than 0.4 μm . All fibres displayed an aspect ratio greater than 3:1, and 31% were coated with ABs. ABs consist of a mixture of Fe-containing proteins (ferritin and hemosiderin), goethite and apatite. ABs apparently nucleate only at the surface of fibres longer than 10 μm and thinner than 0.5 μm . These fibres display L and W values that are very close to the “Stanton-size parameters” ($L > 8 \mu\text{m}$ and $W < 0.25 \mu\text{m}$) and they eventually lead to frustrated phagocytosis and chronic inflammation in the alveolar space. The fibre-coating process represents the exocytotic activity of macrophages aimed at the isolation of these fibres by deposition of ferroproteins (*e.g.*, ferritin) onto the fibre surface. The occurrence of goethite in mature ABs attests to the alteration of ferrihydrite inside the ferritin, to the degradation of the protein shell, and to exposure of its iron core. This phenomenon can possibly lead to the release of “safely stored iron” in the extracellular space and may induce an Fe-mediated ROS activation.

Supplementary Materials: The following are available online at www.mdpi.com/xxx/s1, Figure S1: Results of the stability test carried out on a mineral particle during an TEM investigation. Stability tests were performed by observing the same ROI for 2 min. After 2 min under the electron beam of the microscope, the crystalline structure of the mineral particle remains unaltered, and there is no formation of an amorphous phase at the particle edges. (a) Whole picture of the mineral particle. (b) HRTEM image of the mineral particle after 2 min under the electron beam, showing a highly crystalline structure (red square is the ROI). Figure S2: (a) SEM image of non-coated amosite fibre found in the lung tissue of the male subject. SEM image was acquired using the signal of secondary electrons. Fibre is surrounded by residues of incomplete ashing. (b) SEM-EDX spot analysis (white star) of amosite shown in Figure S2a. (c) HRTEM micrograph of an individual non-coated crocidolite fibre found in the lung tissue of the male subject. Crocidolite fibre exhibits a thin amorphous layer on its surface. Red arrows and red lines highlight the amorphous layer. (d) FFT pattern extracted from HRTEM image shown in

S2c, where the red square represents the region of interest. The d-spacings (Å) and the angle determined from the pattern are: $[010] = 17.8 \text{ \AA}$, $[001] = 5.3 \text{ \AA}$, and $\alpha = 90^\circ$. Calculated cell parameters are consistent with the data for the South-African crocidolite (RRUFF ID = R060028) [39]. Figure S3: (a) HRTEM micrograph of partially-coated crocidolite fibre found in the lung tissue of the male subject. Red arrows highlight the ABs segments (b) FFT pattern of the crocidolite fibre shown in Figure S3a, where the red square is the region of interest. The d-spacings (Å) and the angle determined from the pattern are: $[010] = 17.7 \text{ \AA}$, $[001] = 5.3 \text{ \AA}$, and $\alpha = 90^\circ$.

Author Contributions: A.F.G. and D.D.G. conceptualised the research project. A.F.G., D.D.G., A.Z., O.S. and P.B. designed the study and analysed the data. D.D.G. and A. Z. carried out SEM analyses. R.V. and R.G. carried out TEM analyses. P.B. performed the autopsy. O. S. helped during the reconstruction of the working activities of the male subject of this study. All authors contributed to the writing of the manuscript.

Funding: This research was supported by the grant “Fondi di Ateneo per la Ricerca (FAR 2017)—Fiber potential toxicity Index (FPTI). A quantitative model to evaluate the toxicity and pathogenicity of mineral fibers, including asbestos”. The study was further supported in part by grants P30-ES013508 and P42-ES023720 awarded by the National Institute of Environmental Health Sciences (NIEHS). The findings are not the official opinions of NIEHS or NIH. This work was carried out in part at the Singh Center for Nanotechnology, part of the National Nanotechnology Coordinated Infrastructure Program, which is supported by the National Science Foundation grant NNCI-1542153.

Acknowledgments: Anna Somigliana is kindly acknowledged for the ashing treatment of the lung tissue. Mauro Zapparoli is kindly acknowledged for his support during the SEM sessions.

Conflicts of Interest: The authors declare no conflict of interest. The funders had no role in the design of the study; in the collection, analyses, or interpretation of data; in the writing of the manuscript, or in the decision to publish the results.

References

1. Alleman, J.E.; Mossman, B.T. Asbestos revisited. *Sci. Am.* **1997**, *277*(1), 54–57.
2. Gualtieri, A.F. Mineral fibre-based building materials and their health hazards. In *Toxicity of Building Materials*; Woodhead Publishing: Cambridge, UK, 2012; pp. 166–195.
3. Dichicco, M.C.; Paternoster, M.; Rizzo, G.; Sinisi, R. Mineralogical asbestos assessment in the southern Apennines (Italy): A review. *Fibers.* **2019**, *7*, 24.
4. Schumacher, J.C.; Welch, M.D.; Hawthorne, F.C.; Oberti, R.; Harlow, G.E.; Maresch, W.V.; Martin, R.F. Nomenclature of the amphibole supergroup. *Am. Miner.* **2012**, *97*, 2031–2048.
5. Ballirano, P.; Bloise, A.; Lezzerini, M.; Pacella, A.; Perchiazzi, N.; Dogan, M.; Dogan, A.; Gualtieri, A. The crystal structure of mineral fibres. In *Mineral Fibres: Crystal Chemistry, Chemical-Physical Properties, Biological Interaction and Toxicity*; Mineralogical Society of Great Britain and Ireland: London, United Kingdom, 2017; pp. 17–64.
6. Gualtieri, A.F. *Mineral Fibres: Crystal Chemistry, Chemical-Physical Properties, Biological Interaction and Toxicity*; Mineralogical Society of Great Britain and Ireland: London, United Kingdom, 2017, pp. 1–533.
7. Niklinski, J.; Niklinska, W.; Chyczewska, E.; Laudanski, J.; Naumnik, W.; Chyczewski, L.; Pluygers, E. The epidemiology of asbestos-related diseases. *Lung Cancer* **2004**, *45*, S7–S15.
8. IARC (International Agency for Research on Cancer). Asbestos (chrysotile, amosite, crocidolite, tremolite, actinolite, and anthophyllite). *IARC Monogr Eval Carcinog Risks Hum. C.* **2012**, *100*, 219–309.
9. Capella, S.; Belluso, E.; Bursi, N.; Tibaldi, E.; Mandrioli, D.; Belpoggi, F.; Gualtieri, A. *In vivo* biological activity of mineral fibres. In *Mineral Fibres: Crystal Chemistry, Chemical-Physical Properties, Biological Interaction and Toxicity*; Mineralogical Society of Great Britain and Ireland: London, United Kingdom, 2017; pp. 307–345.
10. Asgharian, B.; Hofmann, W.; Miller, F. Mucociliary clearance of insoluble particles from the tracheobronchial airways of the human lung. *J. Aerosol Sci.* **2001**, *32*, 817–832.
11. E.; Lehnert, B. Pulmonary and thoracic macrophage subpopulations and clearance of particles from the lung. *Environ. Heal. Perspect.* **1992**, *97*, 17–46.

12. Schlosser, P.; Asgharian, B.; Medinsky, M. Inhalation Exposure and Absorption of Toxicants. In *Comprehensive Toxicology*; Elsevier BV, Amsterdam, The Netherlands, 2010; pp. 75–109.
13. Donaldson, K.; Murphy, F.A.; Duffin, R.; Poland, C.A. Asbestos, carbon nanotubes and the pleural mesothelium: a review of the hypothesis regarding the role of long fibre retention in the parietal pleura, inflammation and mesothelioma. *Part. Fibre Toxicol.* **2010**, *7*, 5.
14. WHO (World Health Organization). *Determination of Airborne Fibre Number Concentrations: A Recommended Method, by Phase Contrast Optical Microscopy (Membrane Filter Method)*; World Health Organization: Geneva, Switzerland, 1997; pp. 1–53.
15. Gualtieri, A.F. Towards a quantitative model to predict the toxicity/pathogenicity potential of mineral fibers. *Toxicol. Appl. Pharmacol.* **2018**, *361*, 89–98.
16. Gualtieri, A.F.; Pollastri, S.; Gandolfi, N.B.; Gualtieri, M.L. *In vitro* acellular dissolution of mineral fibres: A comparative study. *Sci. Rep.* **2018**, *8*, 7071.
17. Gualtieri, A.F.; Gandolfi, N.B.; Pollastri, S.; Burghammer, M.; Tibaldi, E.; Belpoggi, F.; Pollok, K.; Langenhorst, F.; Vigliaturo, R.; Dražić, G. New insights into the toxicity of mineral fibres: A combined in situ synchrotron μ -XRD and HR-TEM study of chrysotile, crocidolite, and erionite fibres found in the tissues of Sprague-Dawley rats. *Toxicol. Lett.* **2017**, *274*, 20–30.
18. Bursi Gandolfi, N.; Gualtieri, A.F.; Pollastri, S.; Tibaldi, E.; Belpoggi, F. Assessment of asbestos body formation by high resolution FEG-SEM after exposure of Sprague-Dawley rats to chrysotile, crocidolite, or erionite. *J. Hazard. Mater.* **2016**, *306*, 95–104.
19. Haque, A.K.; Kanz, M.F. Asbestos bodies in children's lungs: An association with sudden infant death syndrome and bronchopulmonary dysplasia. *Arch. Pathol. Lab. Med.* **1988**, *112*, 514–518.
20. Pooley, F. Asbestos Bodies, Their formation, Composition and Character. *Environ. Res.* **1972**, *5*, 363–379.
21. Davis, J.M.G. Electron-Microscope Studies of Asbestosis in Man and Animals. *Ann. New York Acad. Sci.* **1965**, *132*, 98–111.
22. Suzuki, Y.; Churg, J. Structure and development of the asbestos body. *Am. J. Pathol.* **1969**, *55*, 79–107.
23. Suzuki, Y.; Churg, J. Formation of the asbestos body a comparative study with three types of asbestos. *Environ. Res.* **1970**, *3*, 107–118.
24. Koerten, H.K.; Hazekamp, J.; Kroon, M.; Daems, W.T. Asbestos body formation and iron accumulation in mouse peritoneal granulomas after the introduction of crocidolite asbestos fibres. *Am. J. Pathol.* **1990**, *136*, 141–157.
25. Morgan, A.; Holmes, A. Concentrations and dimensions of coated and uncoated asbestos fibres in the human lung. *Occup. Environ. Med.* **1980**, *37*, 25–32.
26. Mossman, B.; Pugnali, A.; Gualtieri, A. *In vitro* biological activity and mechanisms of lung and pleural cancers induced by mineral fibres. In *Mineral Fibres: Crystal Chemistry, Chemical-Physical Properties, Biological Interaction and Toxicity*; Mineralogical Society of Great Britain and Ireland: London, United Kingdom, 2017; pp. 261–306.
27. Pollastri, S.; Gualtieri, A.F.; Vigliaturo, R.; Ignatyev, K.; Strafella, E.; Pugnali, A.; Croce, A. Stability of mineral fibres in contact with human cell cultures. An in situ μ XANES, μ XRD and XRF iron mapping study. *Chemosphere* **2016**, *164*, 547–557.
28. Bernstein, D.M.; Rogers, R.; Smith, P.; Chevalier, J. The Toxicological Response of Brazilian Chrysotile Asbestos: A Multidose Subchronic 90-Day Inhalation Toxicology Study with 92-Day Recovery to Assess Cellular and Pathological Response. *Inhal. Toxicol.* **2006**, *18*, 313–332.
29. Bernstein, D.; Dunnigan, J.; Hesterberg, T.; Brown, R.; Velasco, J.A.L.; Barrera, R.; Hoskins, J.; Gibbs, A. Health risk of chrysotile revisited. *Crit. Rev. Toxicol.* **2013**, *43*, 154–183.
30. Langer, A.M.; Nolan, R.P. Chrysotile Biopersistence in the Lungs of Persons in the General Population and Exposed Workers. *Environ. Heal. Perspect.* **1994**, *102*, 235.
31. Pooley, F. An examination of the fibrous mineral content of asbestos lung tissue from the Canadian chrysotile mining industry. *Environ. Res.* **1976**, *12*, 281–298.

32. Kolanjiyil, A.V.; Kleinstreuer, C.; Kleinstreuer, N.C.; Pham, W.; Sadikot, R.T. Mice-to-men comparison of inhaled drug-aerosol deposition and clearance. *Respir. Physiol. Neurobiol.* **2019**, *260*, 82–94.
33. Ménache, M.G.; Miller, F.J.; Raabe, O.G. Particle Inhalability Curves for Humans and Small Laboratory Animals*. *Ann. Occup. Hyg.* **1995**, *39*, 317–328.
34. Barbieri, P.G.; Mirabelli, D.; Somigliana, A.; Cavone, D.; Merler, E. Asbestos Fibre Burden in the Lungs of Patients with Mesothelioma Who Lived Near Asbestos-Cement Factories. *Ann. Occup. Hyg.* **2012**, *56*, 660–670.
35. NIMH (National Institute of Mental Health). 2018. ImageJ. Available online: <https://imagej.nih.gov/ij/> (Accessed on 19 September 2018).
36. Gatan. (2015). Gatan Microscopy Suite Software. Available online: <http://www.gatan.com/products/temanalysis/gatan-microscopy-suite-software>. (Accessed on 2 August 2019).
37. Koerten, H.K., de Bruijn, J.D.; Daems, W. Th. The Formation of Asbestos Bodies by Mouse Peritoneal Macropages. An In Vitro Study. *Am. J. Pathol.* **1990**, *137*, 121–133.
38. Della Ventura, G.; Vigliaturo, R.; Gieré, R.; Pollastri, S.; Gualtieri, A.F.; Iezzi, G. Infra Red Spectroscopy of the Regulated Asbestos Amphiboles. *Minerals* **2018**, *8*, 413.
39. Hawthorne, F.C. The crystal chemistry of the amphiboles. VIII. The crystal structure and site chemistry of fluor-riebeckite. *Can. Miner.* **1978**, *16*, 187–194.
40. Rinaudo, C.; Croce, A.; Musa, M.; Fornero, E.; Allegrina, M.; Trivero, P.; Bellis, D.; Sferch, D.; Toffalorio, F.; Veronesi, G.; et al. Study of Inorganic Particles, Fibers, and Asbestos Bodies by Variable Pressure Scanning Electron Microscopy with Annexed Energy Dispersive Spectroscopy and Micro-Raman Spectroscopy in Thin Sections of Lung and Pleural Plaque. *Appl. Spectrosc.* **2010**, *64*, 571–577.
41. Davis, J.M.G. The ultra-structure of asbestos bodies from human lung. *Brit. J. Exp. Pathol.* **1964**, *45*, 642–646.
42. Richter, G.W. Electron Microscopy of Hemosiderin: Presence of Ferritin and Occurrence of Crystalline Lattices in Hemosiderin Deposits. *J. Cell Boil.* **1958**, *4*, 55–58.
43. Pascolo, L.; Gianoncelli, A.; Schneider, G.; Salomé, M.; Schneider, M.; Calligaro, C.; Kiskinova, M.; Melato, M.; Rizzardi, C. The interaction of asbestos and iron in lung tissue revealed by synchrotron-based scanning X-ray microscopy. *Sci. Rep.* **2013**, *3*, 1123.
44. Jian, N.; Dowle, M.; Horniblow, R.D.; Tselepis, C.; Palmer, R.E. Morphology of the ferritin iron core by aberration corrected scanning transmission electron microscopy. *Nanotechnology* **2016**, *27*, 46.
45. Bardelli, F.; Veronesi, G.; Capella, S.; Bellis, D.; Charlet, L.; Cedola, A.; Belluso, E. New insights on the biomineralisation process developing in human lungs around inhaled asbestos fibres. *Sci. Rep.* **2013**, *7*, 44862.
46. Oury, T.D.; Sporn, T.A.; Roggli, V.L. *Pathology of Asbestos-Associated Diseases*; Springer: Berlin, Germany, 2014; pp. 357.
47. Drits, V.A.; Sakharov, A.; Salyn, L.; Manceau, A. Structural model of ferrihydrite. *Clay. Miner.* **1993**, *28*, 185–207.
48. Gualtieri, A.F.; Venturelli, P. In situ study of the goethite-hematite phase transformation by real time synchrotron powder diffraction. *Am. Mineral.* **1990**, *84*, 895–904.
49. Carlson, L.; Schwertmann, U. Natural ferrihydrites in surface deposits from Finland and their association with silica. *Geochim. Cosmochim. Acta.* **1980**, *45*, 421–429.
50. Cudennec, Y.; Lecerf, A. The transformation of ferrihydrite into goethite or hematite, revisited. *J. Solid State Chem.* **2006**, *179*, 716–722.
51. Davis, J. Asbestos dust as a nucleation center in the calcification of old fibrous tissue lesions, and the possible association of this process to the formation of asbestos bodies. *Exp. Mol. Pathol.* **1970**, *12*, 133–147.
52. Roggli, V.L. The So-called Short-Fiber Controversy: Literature Review and Critical Analysis. *Arch. Pathol. Lab. Med.* **2015**, *139*, 1052–1057.

53. Stanton, M.F.; Layard, M.; Tegeris, A.; Miller, E.; May, M.; Morgan, E.; Smith, A. Relation of Particle Dimension to Carcinogenicity in Amphibole Asbestoses and Other Fibrous Minerals. *J. Natl. Cancer Inst.* **1981**, *67*, 965–975.
54. Churg, A. Asbestos lung burden and disease pattern in man. *Rev. Mineral Geochem.* **1993**, *28*, 409–426.
55. Roggli, V.L.; Green, C.L. Dimensions of elongated mineral particles: A study of more than 570 fibers from more than 90 cases with implications for pathogenicity and classification as asbestiform vs. cleavage fragments. *Ultrastruct. Pathol.* **2019**, *43*, 1–5.
56. Berman, D.W.; Crump, K.S. A Meta-Analysis of Asbestos-Related Cancer Risk That Addresses Fiber Size and Mineral Type. *Crit. Rev. Toxicol.* **2008**, *38*, 49–73.
57. Gunter, M.E.; Belluso, E.; Mottana, A. Amphiboles: Environmental and Health Concerns. *Rev. Miner. Geochem.* **2007**, *67*, 453–516.
58. Mace, M.L.; McLemore, T.L.; Roggli, V.; Brinkley, B.; Greenberg, S.D. Scanning electron microscopic examination of human asbestos bodies. *Cancer Lett.* **1980**, *9*, 95–104.
59. Krombach, F.; Münzing, S.; Allmeling, A.-M.; Gerlach, J.T.; Behr, J.; Dörger, M. Cell Size of Alveolar Macrophages: An Interspecies Comparison. *Environ. Heal. Perspect.* **1997**, *105*, 1261.
60. Suzuki, Y. Interaction of asbestos with alveolar cells. *Environ. Heal. Perspect.* **1974**, *9*, 241–252.
61. Botham, S.K.; Holt, P.F. The mechanism of formation of asbestos bodies. *J. Pathol. Bacteriol.* **1968**, *96*, 443–453.
62. Padmore, T.; Stark, C.; Turkevich, L.A.; Champion, J.A. Quantitative analysis of the role of fiber length on phagocytosis and inflammatory response by alveolar macrophages. *Biochim. Biophys. Acta. Gen. Subj.* **2017**, *1861*, 58–67.
63. Ishida, T.; Fujihara, N.; Nishimura, T.; Funabashi, H.; Hirota, R.; Ikeda, T.; Kuroda, A. Live-cell imaging of macrophage phagocytosis of asbestos fibers under fluorescence microscopy. *Genes Environ.* **2019**, *41*, 14.
64. Fubini, B.; Barceló, F.; Areán, C.O. Ferritin Adsorption on Amosite Fibers: Possible Implications in the Formation and Toxicity of Asbestos Bodies. *J. Toxicol. Environ. Heal. Part A* **1997**, *52*, 343–352.
65. Munro, H.N.; Linder, M.C. Ferritin: Structure, biosynthesis, and role in iron metabolism. *Physiol. Rev.* **1978**, *58*, 317–396.
66. Arosio, P.; Levi, S.; Ferritin, Iron Homeostasis, And Oxidative Damage. *Free Radic. Biol. Med.* **2002**, *4*, 457–463.
67. Cozzi, A.; Santambrogio, P.; Levi, S.; Arosio, P. Iron detoxifying activity of ferritin. Effects of H and L human apoferritins on lipid peroxidation in vitro. *FEBS Lett.* **1990**, *277*, 119–122.
68. Lee, M.; Arosio, P.; Cozzi, A.; Chasteen, N.D. Identification of the EPR-Active Iron-Nitrosyl Complexes in Mammalian Ferritins. *Biochemistry* **1994**, *33*, 3679–3687.
69. Pérez-Arellano, J.L.; García, J.E.L.; Macías, M.C.G.; Gómez, F.G.; López, A.J.; De Castro, S. Hemosiderin-laden macrophages in bronchoalveolar lavage fluid. *Acta Cytol.* **1992**, *36*, 26–30.
70. Roy, S.; Ray, M.R.; Basu, C.; Lahiri, P.; Lahiri, T. Abundance of siderophages in sputum: Indicator of an adverse lung reaction to air pollution. *Acta Cytol.* **2001**, *45*, 958–964.
71. Becroft, D.M.; Lockett, B.K. Intra-alveolar pulmonary siderophages in sudden infant death: A marker for previous imposed suffocation. *Pathology* **1997**, *29*, 60–63.
72. Ghio, A.J.; Churg, A.; Roggli, V.L. Review: Ferruginous Bodies: Implications in the Mechanism of Fiber and Particle Toxicity. *Toxicol. Pathol.* **2004**, *32*, 643–649.

73. Pascolo, L.; Borelli, V.; Canzonieri, V.; Gianoncelli, A.; Birarda, G.; Bedolla, D.E.; Salomé, M.; Vaccari, L.; Calligaro, C.; Cotte, M.; et al. Differential protein folding and chemical changes in lung tissues exposed to asbestos or particulates. *Sci. Rep.* **2015**, *5*, 12129.
74. Gualtieri, A.F.; Di Giuseppe, D.; Zoboli, A.; Lusvardi, G.; Lassinantti Gualtieri, M.; Vigliaturo, R.; Gieré, R.; Bonasoni, P.; Moliterni, A.; Altomare, A.; et al. The lifelong biopersistence of asbestos in the human lungs at the atomic scale. In preparation for IUCrJ.



© 2019 by the authors. Licensee MDPI, Basel, Switzerland. This article is an open access article distributed under the terms and conditions of the Creative Commons Attribution (CC BY) license (<http://creativecommons.org/licenses/by/4.0/>).